https://doi.org/10.1038/s44306-025-00121-z

Entropy-driven phase transition in a non-collinear antiferromagnet due to higher-order exchange interactions

Check for updates

Leo Kollwitz [1] ✉, Moritz A. Goerzen [1,2], Bjarne Beyer [1], Hendrik Schrautzer [3] & Stefan Heinze [1,4]

The 3Q state arises due to the superposition of three symmetry equivalent spin spirals stabilized by higher-order exchange interactions. It has been predicted more than 20 years ago but was only recently discovered in a Mn monolayer on the Re(0001) surface. To date little is known about the thermodynamic properties of this intriguing non-coplanar spin state. Here, we reveal a low-temperature phase transition between the 3Q and the row-wise antiferromagnetic state in this system via Monte Carlo simulations based on an atomistic spin model parametrized by density functional theory. By modeling the free energy landscape in terms of thermal excitations we derive an analytical expression of the partition function, which allows us to prove that the phase transition is driven by entropy. The predicted phase transition is not unique to Mn/Re(0001) but appears for a wide range of magnetic interaction parameters and is expected to occur also for other multi-Q states.

Antiferromagnetic materials have been proposed to play an important role in the future development of spintronic devices[1]. Compared to established ferromagnetic systems, antiferromagnets come with many benefits, including a large robustness against external magnetic fields, absence of internal stray fields, and ultrafast spin dynamics. Recently, non-collinear antiferromagnets have moved into the research focus due to their exceptional topological and dynamical properties[2]. A promising material class are chiral antiferromagnets such as the compounds Mn_3Sn and Mn_3Pt. Recently, it has been demonstrated that their coplanar spin state can be used for room temperature all-antiferromagnetic tunnel junctions[3,4] and that it can be switched by electrical currents via spin-orbit torque[5]. Further, non-coplanar spin alignments are possible in antiferromagnets such as multi-Q states[6] which are linear combinations of spin spiral (1Q) states. Among these, especially the superposition of three row-wise antiferromagnetic (RW-AFM) states, which we here refer to as the 3Q state[7], has recently gained increasing attention due to its topological properties[8–10]. In this spin state, the magnetic moments point along the principle axes of a regular tetrahedron, leading to the presence of topological orbital moments despite a vanishing net spin moment[11,12] even in the absence of spin-orbit coupling. Therefore, the 3Q state exhibits intriguing transport properties in the form of a spontaneous topological Hall effect[9–11,13] and can induce topological superconductivity in magnet-superconductor-hybrid systems[14,15].

Recently, the 3Q state was discovered in a Mn monolayer on the Re(0001) surface using spin-polarized scanning tunneling microscopy experiments[8]. After this initial finding two further ultrathin film systems – Pd/Mn and Rh/Mn bilayers on Re(0001)[16] – and also the bulk material $Co_{1/3}TaS_2$[9,10] have been experimentally verified to host this intriguing magnetic ground state. Even more recently, it has also been observed in magnetic Mn bilayers on Ir(111)[17]. The 3Q state is stabilized in antiferromagnetic films by higher-order exchange interactions such as the biquadratic or the four-spin interactions as has been explained based on density functional theory (DFT) calculations and spin models[7,8,16,18,19]. It has further been demonstrated that the 3Q state can be distorted due to magneto-crystalline anisotropy or topological chiral interactions[12,16].

While many more complex magnetic ground states, which are stabilized by higher-order exchange interactions, have been experimentally observed at low temperatures in ultrathin transition-metal films[20–26] and have also been predicted for two-dimensional van der Waals magnets[27–29], not much is known about the thermal properties of these typically non-collinear magnetic states. It has been previously shown via Monte Carlo (MC) simulations that the introduction of higher-order exchange interactions into a spin model can cause a non-trivial behavior at low temperatures for a system with a ferrimagnetic ground state[30]. However, Monte Carlo simulations including higher-order exchange interactions have so far not been applied to non-collinear antiferromagnets in two-dimensional systems.

Here, we reveal the occurrence of a non-trivial phase transition between the 3Q ground state and the corresponding single-Q state, i.e. the row-wise antiferromagnet, at low temperatures via Monte Carlo simulations based on an atomistic spin model including higher-order interactions. We

[1]Institute of Theoretical Physics and Astrophysics, Kiel University, Kiel, Germany. [2]CEMES, Université de Toulouse, CNRS, Toulouse, France. [3]Science Institute and Faculty of Physical Sciences, University of Iceland, VR-III, Reykjavík, Iceland. [4]Kiel Nano, Surface, and Interface Science (KiNSIS), Kiel University, Kiel, Germany. ✉e-mail: kollwitz@physik.uni-kiel.de

demonstrate that this low-temperature phase transition is driven by entropy and predict that it can be observed in Mn/Re(0001) at temperatures of about 30 K based on using interaction parameters obtained from density functional theory calculations. By varying the interaction constants starting from the DFT values we show that the phase transition is a robust result.

The theoretical framework applied in our work to model the film systems in the relevant temperature regime and to explain the results from Monte Carlo simulations is based on the expansion of the energy landscape around a local energy minimum in the Hessian eigenbasis of the Hamiltonian, which is successfully used in harmonic transition state theory[31,32]. Using this approach, we can explicitly calculate thermodynamical state functions such as the free energy and the entropy which are typically not accessible via Monte Carlo simulations. This method also allows to obtain phase boundaries at a significantly lower computational cost compared to the computationally intense Monte Carlo simulations. An extension of this method is developed here to include unstable eigenmodes, which further widens its applicability and also improves the agreement between the phase diagrams obtained via the theoretical model and the Monte Carlo simulations for the investigated two-dimensional systems.

Results

Atomistic spin model

Understanding the emergence of the 3Q state requires to go beyond the Heisenberg model of pair-wise exchange. In particular, one needs to include higher-order exchange interactions[18]. The strengths of these terms are usually small compared to the pair-wise exchange and are therefore often neglected in the theoretical description. However, they can drastically alter the magnetic ground state of certain material systems by breaking the energy degeneracy of single-Q and multi-Q states. In the past, various experiments have already been conducted which reveal the emergence of such non-trivial magnetic ground states[8,16,20,21,24]. Due to the large number of atoms involved to properly model the experimentally observed behavior of such systems, a purely quantum mechanical treatment is not feasible to date. Therefore, we employ an atomistic spin model, which contains interactions between the magnetic moments derived from a quantum mechanical treatment[18] with interaction parameters obtained from underlying DFT calculations. In this work the system is described within the atomistic spin model using the classical extended Heisenberg Hamiltonian

$$\begin{aligned} H = &- \sum_{i,j} J_{ij}(\mathbf{m}_i \cdot \mathbf{m}_j) - \sum_i K_i(\mathbf{n} \cdot \mathbf{m}_i)^2 \\ &- \sum_{i,j} B_{ij}(\mathbf{m}_i \cdot \mathbf{m}_j)^2 - \sum_{i,j,k} Y_{ijk}[(\mathbf{m}_i \cdot \mathbf{m}_j)(\mathbf{m}_j \cdot \mathbf{m}_k) \\ &+ (\mathbf{m}_j \cdot \mathbf{m}_i)(\mathbf{m}_i \cdot \mathbf{m}_k) + (\mathbf{m}_i \cdot \mathbf{m}_k)(\mathbf{m}_k \cdot \mathbf{m}_j)] \\ &- \sum_{i,j,k,l} F_{ijkl}[(\mathbf{m}_i \cdot \mathbf{m}_j)(\mathbf{m}_k \cdot \mathbf{m}_l) \\ &+ (\mathbf{m}_i \cdot \mathbf{m}_l)(\mathbf{m}_j \cdot \mathbf{m}_k) - (\mathbf{m}_i \cdot \mathbf{m}_k)(\mathbf{m}_j \cdot \mathbf{m}_l)] \end{aligned} \tag{1}$$

where $\mathbf{m}_i$ is a unit vector representing the direction of the magnetic moment at lattice site i. The included interactions are the bilinear exchange (J_{ij}), the magneto-crystalline anisotropy energy (K_i), the biquadratic exchange (B_{ij}) as well as the four-spin three-site (Y_{ijk}) and the four-spin four-site (F_{ijkl}) exchange. The interaction constants were taken from previous DFT calculations[8] for a Mn monolayer in fcc stacking on the Re(0001) surface, denoted as fcc-Mn/Re(0001) in the following (see "Methods" and Supplementary Table 1 for details). We neglect dipole-dipole interactions as they are usually small energy contributions on the order of 0.1 meV/atom and can be effectively included into the magnetocrystalline anisotropy energy (MAE) for film systems[33,34].

For simplicity the Dzyaloshinskii-Moriya interaction (DMI) is not taken into account since it does not affect the 3Q state as it is a superposition of three collinear row-wise antiferromagnetic states. The bilinear exchange as well as DMI energies are linear under superposition, thus the contribution to the ideal 3Q state must vanish as well. This can even be generalized further, as this argument holds for every state along the 2Q-3Q-1Q path which represent distorted 3Q states[12]. Such a distorted 3Q state occurs as the ground state in this system at finite MAE (see Supplementary Note 1 for details). The presence of the DMI in the system can lead to a modulation of the multi-Q ground state, but does not qualitatively affect the observed low temperature phase transition (see Supplementary Note 2).

Monte Carlo simulations

In the case of a Mn monolayer in fcc stacking on the Re(0001) surface the DFT calculations reveal a small energy difference of only $E_{3Q} - E_{RW\text{-}AFM} = -0.7$ meV/Mn atom between the 3Q and the RW-AFM state[8]. Due to this flat energy landscape, we first verify that the magnetic ground states are consistent between the atomistic spin model and the DFT total energy calculations. The ground state within the atomistic spin model is determined using classical Monte Carlo simulations (see "Methods" for details). Distinguishing the presence of a 3Q state from the RW-AFM in the obtained data is not trivial, as both show a vanishing net magnetization. While quantities such as the scalar-spin chirality defined by $\chi_{ijk} = \mathbf{m}_i \cdot (\mathbf{m}_j \times \mathbf{m}_k)$ can be used to distinguish non-coplanar from coplanar states, it fails to also identify the disordered paramagnetic phase. In this work the so-called spin structure factor (SSF) of a magnetic configuration $\mathbf{M}$, defined as

$$S[\mathbf{M}](\mathbf{q}) = \frac{1}{N^2} \sum_{\alpha \in \{x,y,z\}} \left| \sum_{i=1}^{N} m_i^{\alpha} e^{-i\mathbf{q}\cdot\mathbf{r}_i} \right|^2, \tag{2}$$

is used as a general antiferromagnetic order parameter[35]. Here, N is the number of atoms present in the simulation box. This quantity shows the contributions of the spin spiral states with wave vector $\mathbf{q}$ to the magnetic state and corresponds to the intensity measured in inelastic neutron scattering experiments[36]. Its components at the reciprocal lattice vectors $\mathbf{q}_i$, (i = 1, 2, 3), located at the three $\overline{\mathrm{M}}$-points of the first Brillouin zone (BZ), measure the presence of each of the three symmetry-equivalent RW-AFM states in a given state. This makes it a suitable order parameter for the distinctions between the RW-AFM (single-Q) state, showing only one prominent peak on one of the $\overline{\mathrm{M}}$-points, the 3Q state, which shows peaks at all three distinct $\overline{\mathrm{M}}$-points with reduced intensity (Fig. 1a-d), and the paramagnetic phase with nearly vanishing components[35].

For the moment, we assume a vanishing MAE (K = 0) in order to obtain the ideal 3Q state and to avoid the complication of a distorted 3Q state that occurs at finite MAE. However, a finite value of the MAE does not change the character of the phase transition as will be shown in the following. With the DFT interaction parameters from ref. 8 and setting K = 0, the equilibrium state at T = 1 K (Fig. 1e) indeed shows tetrahedron angles of neighboring spins, characteristic for the ideal 3Q state. The average components of the spin structure factor (Fig. 1f) also show prominent peaks on all three $\overline{\mathrm{M}}$-points, with small thermal noise visible. The state was obtained using a simulated annealing approach. For a 60 × 60 simulation box the simulations start from a uniform random spin configuration at T = 1500 K. Using 10^8 single spin updates for the equilibration process at each temperature, the system is annealed to T = 1 K using a total of 150 linearly spaced temperature steps. The obtained state at T = 1 K is assumed to be in the vicinity of the ground state and is then minimized with respect to its energy using the L-BFGS algorithm[37,38] to remove thermal fluctuations, which indeed results in the ideal 3Q alignment.

For the simulation at finite temperatures, the temperature dependence of the SSF at the three distinct $\overline{\mathrm{M}}$-points in the first Brillouin zone is shown in Fig. 2a. The data were obtained from 20 independent Monte Carlo simulations starting at T = 52 K from a previously equilibrated state. The system was annealed to T = 32 K using a total of 200 linearly spaced temperature steps. For each temperature, 4.32×10^7 single spin updates were performed for the equilibration. After that, 2.5×10^4 samples across 1.8×10^8 single spin updates were taken for the computation of the averages. The averaged data of each individual simulation was then averaged again across the 20 independent simulations. For low temperatures T < 43 K the $\overline{\mathrm{M}}$-point components of the SSF are of roughly equal magnitude, indicating the

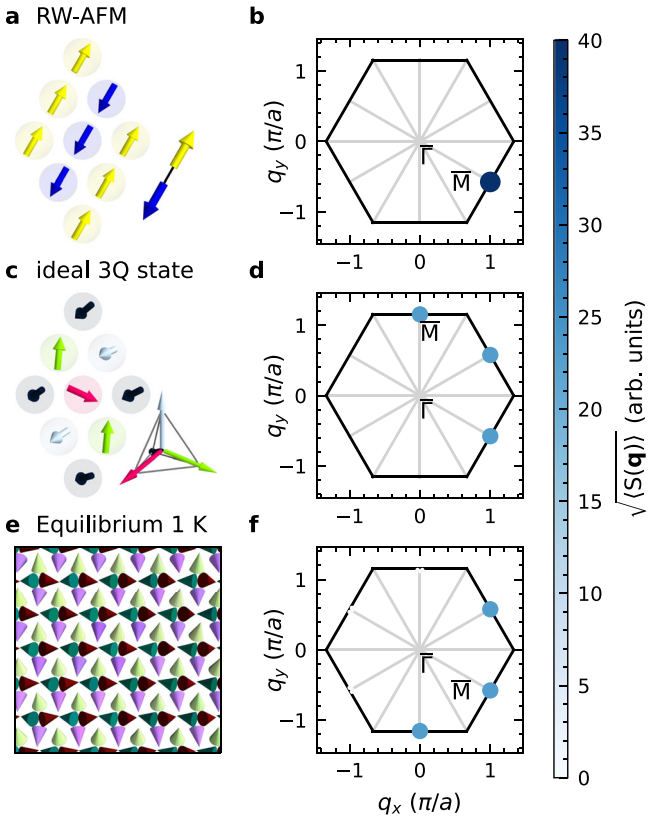


Fig. 1 | Representations of RW-AFM and 3Q state in real and reciprocal space. Schematic real space representation of **a** the RW-AFM on a hexagonal lattice. This single-Q state shows only one prominent component in its spin-structure factor at one of the $\overline{\mathrm{M}}$-points in the first Brillouin zone (see **b**). **c** Non-coplanar ideal 3Q state on the hexagonal 2D atomic lattice and a 3D view of the spin state illustrating the tetrahedral angles between adjacent spins on the lattice. **d** The spin structure factor of the 3Q state shows equally prominent components at all three $\overline{\mathrm{M}}$-points. In **e, f** the equilibrium state at $T = 1$ K obtained via MC simulations as described in the main text and the averaged spin structure factor at this temperature are shown. For the components of the spin structure factor across the first Brillouin zone (**b, d, f**) their color as well as the respective marker size depend on their magnitude.

presence of the 3Q state. Due to the averaging, this could have also been caused by the presence of three RW-AFM domains or the switching from one RW-AFM orientation to another during the simulation. However, the real space representation of exemplary states at different temperatures shows the presence of the 3Q state (Fig. 2b,c) in accordance with the determined ground state. Across the temperature range $43\ \mathrm{K} \leq T \leq 46\ \mathrm{K}$, the system undergoes a phase transition between a 3Q phase present at lower temperatures and the corresponding single-Q (RW-AFM) state present at higher temperatures (Fig. 2d,e). This transition shows the complex and non-trivial effects that higher-order exchange interactions can have on the free energy landscape of the magnetic configurations in Mn/Re(0001).

For the case of a vanishing MAE considered in this section, the Hamiltonian in Eq. (1) is $O(3)$ symmetric. Therefore, one would not expect long-range magnetic order in the thermodynamic limit according to the Mermin-Wagner theorem[39]. However, due to the chirality of the 3Q state, the discrete time reversal symmetry is spontaneously broken, allowing for long range order of the scalar spin chirality at finite temperatures[40]. Similarly, the collinear RW-AFM state, which does not possess a chirality, breaks the C_3 symmetry of the lattice. Due to the finite size of the simulation box, which limits the spin–spin correlation length and introduces an effective magnon gap, even the long-range magnetic order is preserved at finite temperatures. The opening of the magnon gap also happens at finite MAE which is the general case further considered in the following. For a detailed discussion of the finite size effect, see Supplementary Note 3.

Free energy computation

In order to theoretically describe the behavior at finite temperatures of Mn/Re(0001) and to quantify it in terms of the relevant thermodynamic state functions, which here are the (Helmholtz) free energy $\mathcal{F}$, the entropy $\mathcal{S}$ and the internal energy $\mathcal{U}$, an analytical expression for the partition function $\mathcal{Z}$ of an ensemble of magnetic configurations is needed. This can be achieved within the framework of the harmonic approximation (HA) of the energy landscape around some local energy minimum state. Here, we will give a brief outline of this framework, which is described in detail in ref. 41. In a second order approximation to the Hamiltonian (Eq. (1)) magnetic excitations can be expressed in the eigenbasis of its Hessian, which contains the second derivatives of the energy with respect to variations of the magnetic configuration. It has to be noted, that this basis resembles an orthonormal basis in spin space and thus is a computational affordable choice of a coordinate system for the computation of ensemble averages, needed for estimations of free energy. The eigenvectors thus do not resemble physical excitations of the magnetic texture, such as magnons. The corresponding eigenvectors are commonly divided into harmonic modes and zero modes, which are characterized by their respective eigenvalue $\lambda > 0$ or $\lambda = 0$. The harmonic modes are modeled by a quadratic energy dispersion along their normal coordinate p, while the zero modes – corresponding to symmetries of the Hamiltonian – explicitly contribute with their entire configuration space volume ζ. This leads to the approximate expression of the partition function for an ensemble of configurations $\mathbf{M}$ in the subspace Ψ_0 around a local energy minimum with energy E_0, which reads

$$\mathcal{Z}^{\mathrm{HA}} = \int_{\Psi_0} e^{-\beta E(\mathbf{M})}\,\mathrm{d}\mathbf{M} \tag{3}$$

$$\approx \left(\prod_{n\in\mathbb{K}_{\mathrm{zero}}} \zeta_n\right)\left(\prod_{n\in\mathbb{K}_{\mathrm{harm.}}} \int_{-\infty}^{\infty} e^{-\frac{1}{2}\beta\lambda_n p_n^2}\,\mathrm{d}p_n\right) e^{-\beta E_0} \tag{4}$$

$$= \left(\prod_{n\in\mathbb{K}_{\mathrm{zero}}} \zeta_n\right)\left(\prod_{n\in\mathbb{K}_{\mathrm{harm.}}} \sqrt{\frac{2\pi}{\beta\lambda_n}}\right) e^{-\beta E_0} \tag{5}$$

$$= \mathcal{Z}_{\mathrm{zero}} \cdot \mathcal{Z}_{\mathrm{harm.}} \cdot e^{-\beta E_0} \tag{6}$$

with the usual $\beta = 1/k_{\mathrm{B}}T$. Here $\mathbb{K}_{\mathrm{zero}}$ and $\mathbb{K}_{\mathrm{harm.}}$ are the index sets of the zero and harmonic modes, respectively. Using the harmonic approximation, we are therefore able to give quantitative entropy differences between the involved RW-AFM and 3Q states. Surprisingly, computing the eigenvalues of the Hessian of the RW-AFM state reveals the presence of unstable eigenmodes, characterized by negative eigenvalues $\lambda_n < 0$. Thus, the state is not a local energy minimum, even though it appears as the thermal equilibrium state at finite temperatures.

We can further extend the partition function to describe general stationary points with some number of negative eigenvalues in its Hessian instead of only local energy minima (cf. Fig. 3). Using numerical mode following algorithms[42,43] we can identify two different kinds of unstable modes present in the system. The first kind belonging to the lowest eigenvalues of the Hessian are unstable periodic modes, which are modeled by the dispersion

$$E(p) = -2\epsilon_I \sin^2\left(\frac{1}{2}p\sqrt{\frac{|\lambda|}{\epsilon_I}}\right) \tag{7}$$

with the corresponding eigenvalue $\lambda < 0$ and the absolute inflection point energy $\epsilon_I > 0$ of the dispersion. This energy is defined with respect to $E(p = 0) = 0$. It is determined using the mode following algorithms as the energy of the state along the normal coordinate, at which the corresponding eigenvalue λ vanishes. The second kind of unstable mode is modeled using the

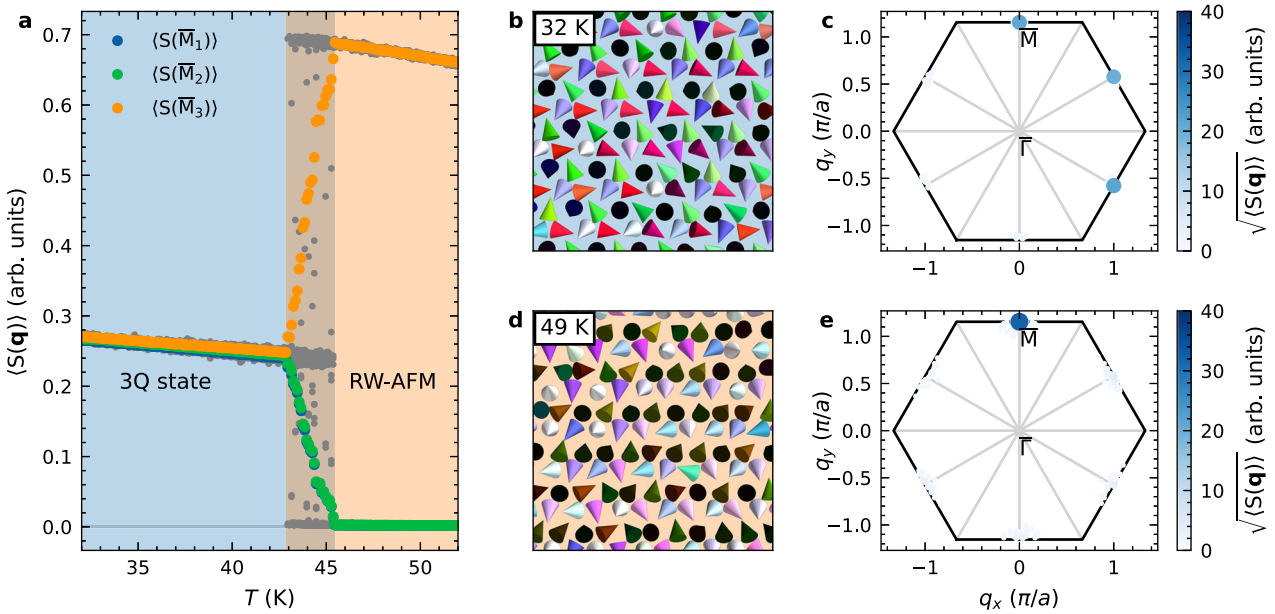


Fig. 2 | Phase transition from the 3Q to the RW-AFM state. a Temperature dependence of the SSF contributions at the three different M̄-points in the first BZ. The colored data points are averaged across 20 independent simulations neglecting MAE, while the gray data points show the results of each individual simulation. For the lower temperatures (blue background) the three SSF contributions are of nearly equal magnitude, while for higher temperatures (orange background) there is only a single prominent component visible. **b**, **d** Exemplary equilibrium states at $T = 32$ K and $T = 49$ K showing a 3Q and a RW-AFM structure, respectively. **c**, **e** Averaged components of the SSF across the entire first BZ at $T = 32$ K and $T = 49$ K respectively.

quartic dispersion

$$E(p) = \frac{1}{2}\lambda p^2 + \frac{5\lambda^2}{144\epsilon_I}p^4 . \tag{8}$$

Again, the different modes are assumed to be independent of one another, so that we can write the partition function in the extended harmonic approximation (EHA) as a product of integrals over the Boltzmann distribution of the corresponding energy dispersions as

$$\mathcal{Z}^{\mathrm{EHA}} = \prod_{\mathrm{modes}} \left(\int_{\mathrm{period}} \mathrm{e}^{-\beta E_{\mathrm{mode}}(p)} \mathrm{d}p \right) \mathrm{e}^{-\beta E_0} \tag{9}$$

$$= \mathcal{Z}_{\mathrm{zero}} \cdot \mathcal{Z}_{\mathrm{harm.}} \cdot \mathcal{Z}_{\mathrm{per.}} \cdot \mathcal{Z}_{\mathrm{quart.}} \cdot e^{-\beta E_0} . \tag{10}$$

Zero and unstable periodic modes have a finite period, over which the integration is performed, while the harmonic and quartic modes are assumed to be non-periodic, thus the integration is performed over the interval $(-\infty, \infty)$. For the modeling of the individual modes and their contributions to the partition function see "Methods". This expression for the partition function lets us derive the free energy $\mathcal{F} = -ln(\mathcal{Z})/\beta$, the internal energy $\mathcal{U} = -\partial_\beta \ln \mathcal{Z}$ and the entropy $\mathcal{S} = (\mathcal{U} - \mathcal{F})/T$ (for explicit formulas see Supplementary Note 4) of different initial configurations such as the RW-AFM and the 3Q state.

Treating the different kinds of modes in the extended harmonic approximation allows us to quantitatively compute the thermodynamic state functions of the 3Q and the RW-AFM state (Fig. 4). At low temperatures, the 3Q state exhibits a lower free energy than the RW-AFM state (Fig. 4a), thus making it the thermodynamically preferred state. However, at $T_c^{\mathrm{EHA}} = 32.7$ K the two curves cross and the RW-AFM becomes favorable compared to the 3Q state, albeit its larger energy (Fig. 4b). Due to the small energy difference between the two states, this transition happens at a temperature well below the transition temperature to the paramagnet, which has been determined to be $T_{\mathrm{PM}} \approx 115$ K (see Supplementary Note 5 and

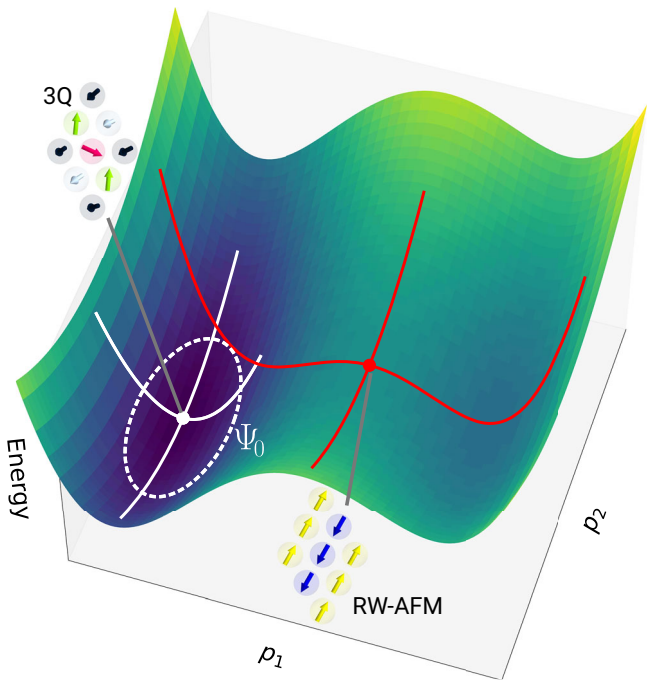


Fig. 3 | Energy landscape around the 3Q and the RW-AFM state. Illustration of the energy landscape using different kinds of Hessian eigenmodes around a local energy minimum (white) or a general stationary point with a negative eigenvalue (red). In the case of fcc-Mn/Re(0001) these correspond to the 3Q and the RW-AFM state.

Supplementary Fig. 7). Comparing the predicted internal energy $\mathcal{U}$ with the one sampled during the Monte Carlo simulations (Fig. 4b) shows a very good agreement for the 3Q as well as the RW-AFM phase with the extended harmonic approximation. For low temperatures, the internal energy in both cases has a nearly linear dependence on the temperature as expected from

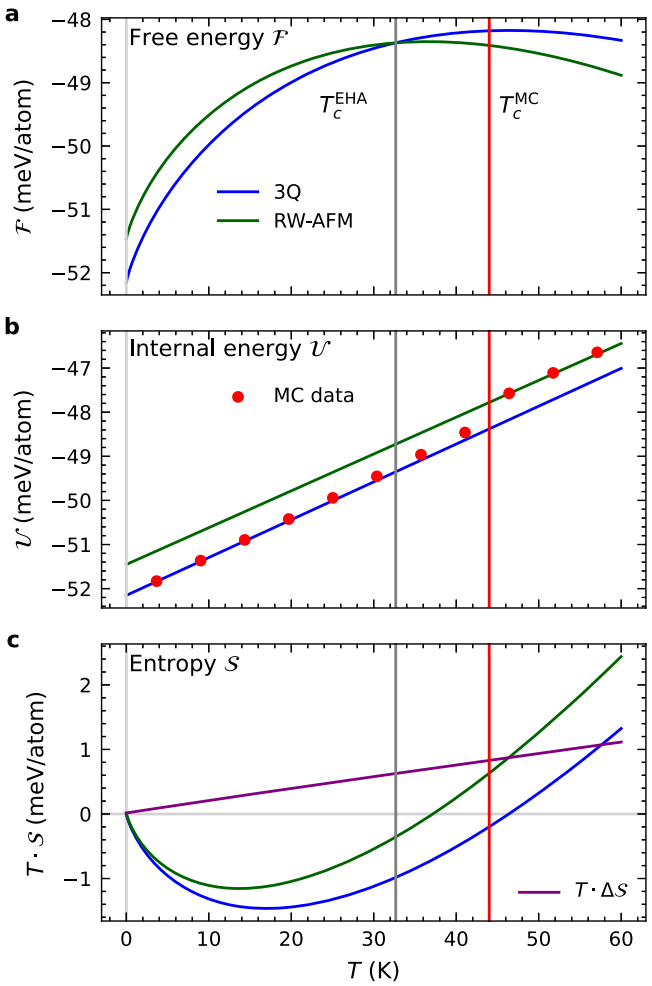


Fig. 4 | Thermodynamic state functions across the phase transition. Temperature dependence of **a** the free energy $\mathcal{F}$, **b** internal energy $\mathcal{U}$ and **c** (temperature scaled) entropy $\mathcal{S}$ for the 3Q state and RW-AFM in fcc-Mn/Re(0001) computed within the extended harmonic approximation. The blue (green) curves show the thermodynamic state functions for the 3Q (RW-AFM state). The vertical lines indicate the transition temperatures obtained within the extended harmonic approximation (gray, $T_c^{\mathrm{EHA}} = 32.7$ K) and the MC simulations (red, $T_c^{\mathrm{MC}} = 44.0$ K). Additionally, data of the internal energy $\mathcal{U}$ obtained from the Monte Carlo simulations is shown for exemplary temperatures in the 3Q as well as a RW-AFM phase. In **c** the (temperature scaled) entropy difference $T \cdot (\mathcal{S}_{\mathrm{RW-AFM}} - \mathcal{S}_{\mathrm{3Q}})$ is shown in purple.

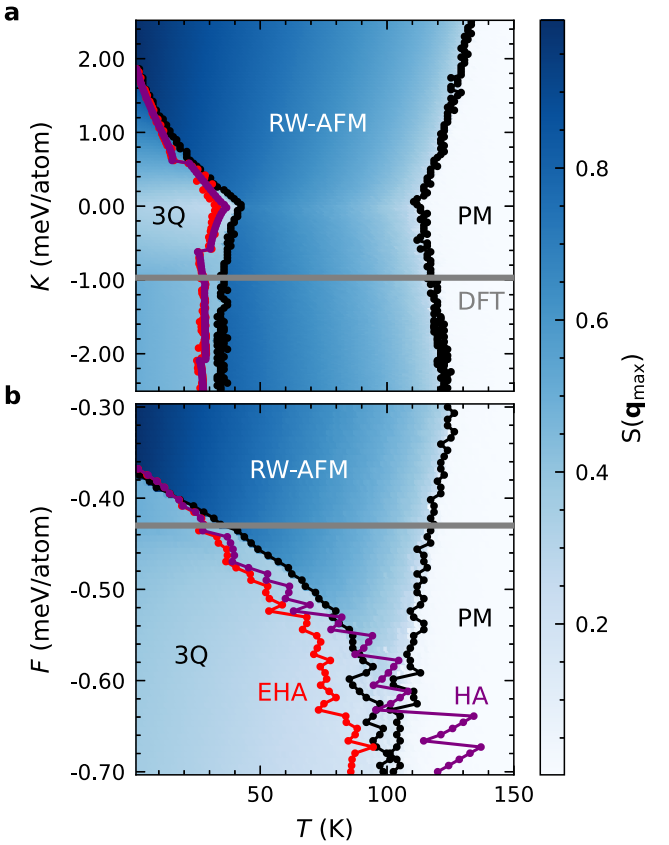


Fig. 5 | Phase diagrams vs. magnetic interaction strengths. Phase diagrams showing the maximum component of the SSF (see color bar) for varied interaction parameters of **a** the MAE and **b** the four-spin four-site exchange. All other interaction constants have been chosen according to the DFT values given in Supplementary Table 1 for fcc-Mn/Re(0001)[8]. The horizontal gray line in panel **a** and **b** indicates the value of the MAE and four-spin four-site interaction constant, respectively, obtained via DFT for fcc-Mn/Re(0001). The black lines show the phase boundaries obtained in the Monte Carlo simulations. The purple (red) phase boundaries between the RW-AFM and 3Q state are obtained within the (extended) harmonic approximation, excluding (including) unstable degrees of freedom.

the equipartition theorem. Computing the entropy of the two states (Fig. 4c) shows the RW-AFM being entropically favored.

This finding is consistent with a previous theoretical study[44] showing single-Q states being favored compared to multi-Q states in the presence of thermal fluctuations. In our case, however, due to the presence of higher-order exchange interactions, there is an energetic difference between the 3Q state and RW-AFM, making the former the equilibrium state at sufficiently low temperatures. The entropy difference at $T_c^{\mathrm{EHA}} = 32.7$ K between the two states is calculated to be $\Delta\mathcal{S} = 1.92 \cdot 10^{-2}$ meV $\cdot$ K^{-1}/atom. Note, that for both states the entropies diverge for $T \to 0$, apparently violating the third law of thermodynamics, which is due to the harmonic approximation not being defined at absolute zero. However, the entropic energy contribution $T\mathcal{S}$ has a finite limit, which is zero if only harmonic modes are present.

So far, we have focused on the magnetic interaction parameters obtained via DFT for a Mn monolayer in fcc stacking on Re(0001) neglecting the magneto-crystalline anisotropy. However, the observed phase transition is stable across a wide range of interaction parameters and allowing critical temperatures of up to 100 K as we have found by varying the interaction strengths in our Monte Carlo simulations (Fig. 5). In particular, the temperature dependence of the largest component of the SSF is shown for varying interaction constants of the MAE (Fig. 5a) and the four-spin four-site exchange (Fig. 5b). For the RW-AFM (single-Q) state this component will be close to unity, while for the ideal 3Q state it is about 1/3. In the disordered paramagnetic (PM) phase the component will be close to zero, allowing for a clear visual difference between the three relevant phases. The obtained phase boundaries from the Monte Carlo simulations are shown in black. The simulation data shown in Fig. 5 has been obtained from a single Monte Carlo simulation for each interaction constant. In order to ensure a correct sampling of the phase boundaries, we also reversed the direction of the temperature sweep, starting from the ground state configuration at $T = 1$ K and increasing the temperature. The resulting phase diagrams showed effectively no difference to the ones shown in Fig. 5.

We find that the phase transition from the 3Q to the RW-AFM state at low temperatures, which we found for vanishing MAE (Fig. 2), is robust upon changing the value of the MAE (Fig. 5a). There is also a very good agreement between the extended harmonic approximation (red), in which the unstable modes in the RW-AFM phase are considered as described above, and the Monte Carlo simulations for both easy-plane ($K < 0$) and easy-axis ($K > 0$) anisotropies. Notable here is the varying magnitude of S in the 3Q phase for different values of K. We find that the presence of the MAE in this particular system leads to a large distortion of the ground state towards a 2Q (1Q) state for easy-plane (easy-axis) anisotropies (see Supplementary Note 1 and Supplementary Figs. 1-3). A similar effect, present

here within the atomistic model of fcc-Mn/Re(0001), has been predicted by DFT calculations to also occur in the hcp-Mn/Re(0001) system[12]. However, this distortion does not qualitatively affect the transition to the RW-AFM phase. When ignoring the contribution from the unstable modes for the RW-AFM state, the purple phase boundary is obtained. In the case of varying MAE, the difference is effectively negligible. This is a result of the small number of unstable modes, which is nearly independent of the value of K.

For the four-spin four-site exchange (Fig. 5b) the extended harmonic approximation captures not only the qualitative shape well, but also the quantitative magnitude of the transition temperatures across various parameter strengths and temperature ranges. In contrast to the MAE, lower values of the four-spin four-site interaction strength F shift the transition towards higher temperatures. This can be explained by an increased stability of the 3Q state compared to the RW-AFM state, which manifests itself in the increasing number of unstable modes present in the latter (see Supplementary Note 6 and Supplementary Fig. 8). This is also visible in the phase boundaries obtained within the HA. Neglecting the contribution of the unstable modes (purple) for low values of F leads to an overestimation of the transition temperature, which might even surpass the transition temperature to the disordered paramagnetic phase.

A jagged shape of the purple phase boundary is visible at higher strength of the four-spin four-site interaction (Fig. 5b), which is caused by discontinuous jumps of the computed transition temperature. These are a result of possibly degenerate eigenvalues of the Hessian of the RW-AFM state abruptly changing their sign with decreasing F. This results in an abrupt change in the number of considered harmonic modes for the purple phase boundary. Comparing this behavior with the extended harmonic approximation (red), which includes the contribution of unstable modes, a much better agreement with the Monte Carlo simulations can be seen. Although there are still notable fluctuations in the obtained transition temperature, they are much less pronounced. These fluctuations as well as the general discrepancy to the Monte Carlo simulations are a result of the approximation of the energy landscape, which may deviate significantly from the original at larger thermal energies. Due to the resulting distortions the assumption of independent modes might also no longer be justified. Further, a changing sign of some highly degenerate eigenvalues still leads to a drastic change in the modeling of the respective modes. Nonetheless, the harmonic approximation with the inclusion of unstable modes captures the trend of the phase boundaries between the 3Q and the RW-AFM state very well, especially in the low temperature regime $T \lesssim 50$ K.

Discussion

Based on atomistic Monte Carlo simulations for the Mn monolayer on a Re(0001) substrate using a spin model parameterized from DFT, we predict the occurrence of a low-temperature phase transition between the 3Q ground state and the RW-AFM state. This phase transition, which occurs in addition to that to the paramagnetic phase at the Néel temperature, is induced by the presence of higher-order exchange interactions, which leads to a splitting of the energy degeneracies in the bilinear exchange interactions between the RW-AFM and the 3Q state. Our results show the crucial influence of these higher-order interactions in the finite temperature behavior of Mn/Re(0001) in addition to causing a non-coplanar multi-Q ground state. This highlights the importance of the consideration of these higher-order interactions despite their small energy scale compared to the bilinear exchange.

Modeling the energy landscape in the vicinity of the different spin states, we are able to quantitatively compute all relevant thermodynamic state functions, which are in general not accessible using standard Monte Carlo techniques. The resulting phase boundaries are in very good agreement with Monte Carlo simulations not only for the initial parameter set obtained from DFT, but across a wide range of different interaction strengths as well, while requiring only a small fraction of the computational cost. This for one showcases the robustness of the predicted phase transition against the initial parametrization, but also highlights the accuracy of our theoretical model. By going beyond the harmonic approximation, we are able to include states containing unstable Hessian eigenmodes, which still play an important role in the thermodynamic behavior of this system, as seen from the occurrence of the RW-AFM state as the equilibrium state at finite temperatures. The extended harmonic approximation provides useful insights to the finite temperature behavior of a system by allowing for a fast comparison of the thermodynamic state functions of different relevant states, which are usually already known from prior DFT studies. This model can also be easily extended to include other kinds of interactions in the Hamiltonian e.g. topological-chiral interactions[12,45].

Based on our investigation, this first order phase transition between the 3Q ground state and the entropically favored RW-AFM state can occur, if these two states are energetically close to each other, such that $\Delta\mathcal{U}/\Delta\mathcal{S} < T_c$, with the critical temperature T_c marking the transition to the disordered paramagnetic phase. The 3Q state has also been experimentally observed in a Pd/Mn bilayer on Re(0001)[16]. However, in this system, the condition is not fulfilled since the energetic difference to the RW-AFM state obtained via DFT[16] is by far too large for an additional phase transition to occur, as we have confirmed by Monte Carlo simulations as well as the harmonic approximation (see Supplementary Note 7 and Supplementary Figs. 9 and 10).

Previously, a first-order phase transition has been reported from a ferrimagnetic to a Néel state that can be induced in the presence of higher-order interactions[30] using DFT parameters obtained for a free-standing (unsupported) V monolayer[46]. It was argued that an entropic difference between the two states is the origin of the transition[30], however, without providing calculations of the free energy or the entropy. Our work, on the other hand, is based on realistic magnetic interaction strengths from an underlying DFT parametrization of an already experimentally realized ultrathin film system with a non-collinear magnetic ground state[8,47]. Further, the entropy-driven mechanism of the transition is explicitly demonstrated by the extended harmonic approximation. Note, that a similar phase transition as predicted in our work for two-dimensional systems has recently been observed experimentally in the bulk van-der-Waals material $Co_{1/3}TaS_2$ using transport and neutron scattering measurements[9,10].

For the fcc-Mn/Re(0001) film system, there is a discrepancy in the magnetic ground state between the DFT total energy calculations for the pseudomorphic Mn monolayer and spin-polarized scanning tunneling microscopy experiments, which show a row-wise antiferromagnetic ground state[8]. Recently, it has been demonstrated that this difference is due to the fact that the Mn monolayer actually exhibits a lateral shift with respect to the surface[48] that had not been considered before. Upon taking this structural effect into account in DFT calculations the RW-AFM state is energetically lower than the 3Q state in agreement with experiments[48].

On the other hand, the closely related hcp-Mn/Re(0001) film system exhibits an experimentally verified 3Q ground state[8]. While the DFT total energy calculations are consistent with this experimentally observed ground state, the DFT parametrization of the atomistic spin model (Eq. (1)) suffers from large frustration effects and a shallow energy landscape in the explicit consideration of higher-order exchange interactions. Therefore, in Monte Carlo simulations, we do not obtain the 3Q state at the lowest temperature. Nevertheless, since the phase transition from the 3Q to the RW-AFM state is robust against changes in the parametrization of the spin model and hcp-Mn/Re(0001) possesses an even smaller total energy difference $\Delta\mathcal{U}$ between the 3Q and the RW-AFM state in the DFT calculations[8] than fcc-Mn/Re(0001), it is a promising candidate to experimentally verify the intriguing non-trivial behavior at low temperatures predicted here for ultrathin antiferromagnetic films with a 3Q ground state, e.g. using spin-polarized scanning tunneling microscopy at variable temperatures[49].

The ability to thermally switch between the chiral 3Q state and the collinear row-wise antiferromagnetic (RW-AFM) state can also provide improved control on adatom motion and growth of nanostructures on such magnetic surfaces[48,50], which is potentially useful for the construction of

nanoscale spintronic devices. Based on our work, we further expect that a similar phase transition can occur in two-dimensional magnets from other multi-Q states, e.g. the ↑↑↓↓ states[22,23], to their corresponding single-Q states.

Methods

Magnetic interaction constants of the spin model

For the interaction constants of the atomistic spin model given by Eq. (1), we have chosen the parameters obtained via DFT calculations for a Mn monolayer in fcc stacking on the Re(0001) surface (denoted as fcc-Mn/Re(0001)) given in ref. 8 and summarized in Supplementary Table 1. In these DFT calculations the 3Q state is found as the energetically lowest state. Experimentally, the corresponding 1Q state, i.e. the RW-AFM state, has been observed using spin-polarized scanning tunneling microscopy[8]. This discrepancy between theory and experiment has only recently been resolved[48]. It has been demonstrated that there is a structural lateral shift of the Mn monolayer in the RW-AFM state which lowers its energy below that of the 3Q state leading to a consistent picture of theory and experiment.

For a Mn monolayer in hcp stacking on the Re(0001) surface (denoted as hcp-Mn/Re(0001)) a 3Q state has been observed in the spin-polarized scanning tunneling microscopy experiments of Spethmann et al.[8]. DFT calculations for hcp-Mn/Re(0001) also obtain the 3Q state as energetically lowest with respect to all 1Q (spin spiral) states[8]. However, based on the atomistic spin model parameterized from these DFT calculations we could not stabilize the 3Q state at low temperatures in Monte Carlo (see Supplementary Note 8). We attribute this result to the strong frustration of higher-order exchange interactions in this system which can be seen from the small energy difference between the 3Q and 1Q state on the order of 1 meV/Mn atom found in DFT[8].

Monte Carlo simulations

In order to simulate the system at finite temperatures, we employ classical Monte Carlo simulations using a single-spin updating scheme. For the spin flip mechanism, an adaptive algorithm proposed in ref. 51 has been employed, ensuring an acceptance probability of approximately 50% for each temperature after equilibration. The acceptance probability A to transition from a state $\mathbf{M}$ to the state $\mathbf{M}'$ for each Monte Carlo step is that of the Metropolis algorithm

$$A(\mathbf{M} \to \mathbf{M}') = \min\{1, e^{-\beta(E(\mathbf{M}')-E(\mathbf{M}))}\}\,. \tag{11}$$

The Monte Carlo simulations consist of an initial equilibration of the system at each temperature step. After thermal equilibrium is reached, the measured quantities are computed after every $n_{\text{cycle}} > N$ single spin updates to reduce correlation between them, with N being the number of spins in the simulation box. The mean of the obtained quantities is then taken as the thermal average $\langle \ldots \rangle$. For increased accuracy, a number of statistically independent simulations differing in the seed value of the used Mersenne-twister random-number-generator are performed. The thermal average is then taken as the arithmetic mean of the averages obtained from each individual simulation. All simulations are conducted using periodic boundary conditions.

Harmonic approximation

The individual contributions of the periodic unstable modes can be computed as

$$w \int_{1\text{ period}} \mathrm{e}^{2\beta\epsilon_I \sin^2\left(\frac{1}{2}p\sqrt{\frac{|\lambda|}{\epsilon_I}}\right)}\,\mathrm{d}p \tag{12}$$

$$= w \int_0^{2\pi\sqrt{\frac{\epsilon_I}{|\lambda|}}} \mathrm{e}^{2\beta\epsilon_I \sin^2\left(\frac{1}{2}p\sqrt{\frac{|\lambda|}{\epsilon_I}}\right)}\,\mathrm{d}p \tag{13}$$

$$= 2w\sqrt{\frac{\epsilon_I}{|\lambda|}} \int_0^{\pi} e^{2\beta\epsilon_I \sin^2(\phi)}\,\mathrm{d}\phi \tag{14}$$

$$= 2w\pi\sqrt{\frac{\epsilon_I}{|\lambda|}} e^{2\beta\epsilon_I} I_0^e(\beta\epsilon_I)\,, \tag{15}$$

with w being the number of periods until the initial spin configuration is reached again and $I_\nu^e(z) = e^{-|\Re(z)|} I_\nu(z)$ is the exponentially scaled modified Bessel function of first kind. Similarly, the contribution of one unstable quartic mode evaluates to

$$\int_{-\infty}^{\infty} e^{\frac{\beta|\lambda|}{2}p^2 - \frac{5\beta|\lambda|^2}{144\epsilon_I}p^4}\,\mathrm{d}p \tag{16}$$

$$= \frac{3\pi}{\sqrt{5}}\sqrt{\frac{\epsilon_I}{|\lambda|}} e^{\frac{9}{5}\beta\epsilon_I}\left[I^e_{-\frac{1}{4}}\left(\frac{9}{10}\beta\epsilon_I\right) + I^e_{\frac{1}{4}}\left(\frac{9}{10}\beta\epsilon_I\right)\right]. \tag{17}$$

For a comparison of the dispersions used in the extended harmonic approximation with the ones explicitly computed using numerical mode following and the contribution of the different kinds of modes, see Supplementary Note 9.

Data availability

All relevant data are available from the corresponding authors upon reasonable request.

Code availability

All relevant code is available from the corresponding authors upon reasonable request.

Received: 23 July 2025; Accepted: 12 November 2025;
Published online: 09 January 2026

References

1. Baltz, V. et al. Antiferromagnetic spintronics. *Rev. Mod. Phys.* **90**, 015005 (2018).
2. Rimmler, B., Pal, B. & Parkin, S. Non-collinear antiferromagnetic spintronics. *Nat. Rev. Mater.* 109–127 (2024).
3. Qin, P. et al. Room-temperature magnetoresistance in an all-antiferromagnetic tunnel junction. *Nature* **485**, 613 (2023).
4. Chen, X. et al. Octupole-driven magnetoresistance in an antiferromagnetic tunnel junction. *Nature* **490**, 613 (2023).
5. Zheng, Z. et al. All-electrical perpendicular switching of chiral antiferromagnetic order. *Nat. Mat.* 1407–1413 (2025).
6. Okubo, T., Chung, S. & Kawamura, H. Multiple-*q* states and the skyrmion lattice of the triangular-lattice heisenberg antiferromagnet under magnetic fields. *Phys. Rev. Lett.* **108**, 017206 (2012).
7. Kurz, P., Bihlmayer, G., Hirai, K. & Blügel, S. Three-dimensional spin structure on a two-dimensional lattice: Mn/Cu(111). *Phys. Rev. Lett.* **86**, 1106 (2001).
8. Spethmann, J. et al. Discovery of magnetic single-and triple-q states in Mn/Re(0001). *Phys. Rev. Lett.* **124**, 227203 (2020).
9. Park, P. et al. Tetrahedral triple-q magnetic ordering and large spontaneous Hall conductivity in the metallic triangular antiferromagnet $Co_{1/3}TaS_2$. *Nat. Commun.* **14**, 8346 (2023).
10. Takagi, H. et al. Spontaneous topological Hall effect induced by non-coplanar antiferromagnetic order in intercalated van der Waals materials. *Nat. Phys.* **19**, 961–968 (2023).
11. Hanke, J.-P. et al. Role of Berry phase theory for describing orbital magnetism: From magnetic heterostructures to topological orbital ferromagnets. *Phys. Rev. B* **94**, 121114 (2016).
12. Haldar, S., Meyer, S., Kubetzka, A. & Heinze, S. Distorted 3q state driven by topological-chiral magnetic interactions. *Phys. Rev. B* **104**, L180404 (2021).

13. Martin, I. & Batista, C. Itinerant electron-driven chiral magnetic ordering and spontaneous quantum Hall effect in triangular lattice models. *Phys. Rev. Lett.* **101**, 156402 (2008).
14. Bedow, J. et al. Topological superconductivity induced by a triple-q magnetic structure. *Phys. Rev. B* **102**, 180504 (2020).
15. Nickel, F. & Heinze, S. Topological properties of magnet-superconductor hybrid systems due to atomic-scale non-coplanar spin textures. *npj Spintron.* **3**, 13 (2025).
16. Nickel, F. et al. Coupling of the triple-q state to the atomic lattice by anisotropic symmetric exchange. *Phys. Rev. B* **108**, L180411 (2023).
17. Saxena, V. et al. Strain-driven domain wall network with chiral junctions in an antiferromagnet. https://doi.org/10.48550/arXiv.2408.12580 (2024).
18. Hoffmann, M. & Blügel, S. Systematic derivation of realistic spin models for beyond-Heisenberg solids. *Phys. Rev. B* **101**, 024418 (2020).
19. Beyer, B. et al. Bilayer triple-q state driven by interlayer higher-order exchange interactions. *Phys. Rev. B* **112**, 094430 (2025).
20. Heinze, S. et al. Spontaneous atomic-scale magnetic skyrmion lattice in two dimensions. *Nat. Phys.* **7**, 713–718 (2011).
21. Yoshida, Y. et al. Conical spin-spiral state in an ultrathin film driven by higher-order spin interactions. *Phys. Rev. Lett.* **108**, 087205 (2012).
22. Romming, N. et al. Competition of Dzyaloshinskii-Moriya and higher-order exchange interactions in Rh/Fe atomic bilayers on Ir(111). *Phys. Rev. Lett.* **120**, 207201 (2018).
23. Krönlein, A. et al. Magnetic ground state stabilized by three-site interactions: Fe/Rh(111). *Phys. Rev. Lett.* **120**, 207202 (2018).
24. Gutzeit, M. et al. Nano-scale collinear multi-q states driven by higher-order interactions. *Nat. Commun.* **13**, 5764 (2022).
25. Gutzeit, M., Drevelow, T., Goerzen, M. A., Haldar, S. & Heinze, S. Spontaneous square versus hexagonal nanoscale skyrmion lattices in Fe/Ir(111). *Phys. Rev. B* **108**, L060405 (2023).
26. Nickel, F. et al. Antiferromagnetic order of topological orbital moments in atomic-scale skyrmion lattices. *npj Spintron.* **3**, 7 (2025).
27. Xu, C. et al. Assembling diverse skyrmionic phases in Fe_3GeTe_2 monolayers. *Adv. Mater.* **34**, 2107779 (2022).
28. Li, P., Yu, D., Liang, J., Ga, Y. & Yang, H. Topological spin textures in 1*T*-phase Janus magnets: interplay between Dzyaloshinskii-Moriya interaction, magnetic frustration, and isotropic higher-order interactions. *Phys. Rev. B* **107**, 054408 (2023).
29. Pan, W. et al. Chiral magnetism in lithium-decorated monolayer $CrTe_2$: Interplay between Dzyaloshinskii-Moriya interaction and higher-order interactions. *Phys. Rev. B* **109**, 214405 (2024).
30. Wieser, R., Vedmedenko, E. & Wiesendanger, R. Entropy-driven phase transition in itinerant antiferromagnetic monolayers. *Phys. Rev. B* **77**, 064410 (2008).
31. Bessarab, P. F., Uzdin, V. M. & Jónsson, H. Harmonic transition-state theory of thermal spin transitions. *Phys. Rev. B* **85**, 184409 (2012).
32. Goerzen, M. A., von Malottki, S., Kwiatkowski, G. J., Bessarab, P. F. & Heinze, S. Atomistic spin simulations of electric-field-assisted nucleation and annihilation of magnetic skyrmions in Pd/Fe/Ir(111). *Phys. Rev. B* **105**, 214435 (2022).
33. Lobanov, I. S., Jónsson, H. & Uzdin, V. M. Mechanism and activation energy of magnetic skyrmion annihilation obtained from minimum energy path calculations. *Phys. Rev. B* **94**, 174418 (2016).
34. Draaisma, H. J. G. & de Jonge, W. J. M. Surface and volume anisotropy from dipole-dipole interactions in ultrathin ferromagnetic films. *J. Appl. Phys.* **64**, 3610–3613 (1988).
35. Gvozdikova, M. & Zhitomirsky, M. A Monte Carlo study of the first-order transition in a Heisenberg fcc antiferromagnet. *JETP Lett.* **81**, 236–240 (2005).
36. Rózsa, L., Simon, E., Palotás, K., Udvardi, L. & Szunyogh, L. Complex magnetic phase diagram and skyrmion lifetime in an ultrathin film from atomistic simulations. *Phys. Rev. B* **93**, 024417 (2016).
37. Nocedal, J. & Wright, S. J.*Numerical Optimization* (Springer, 1999).
38. Ivanov, A. V., Uzdin, V. M. & Jónsson, H. Fast and robust algorithm for energy minimization of spin systems applied in an analysis of high temperature spin configurations in terms of skyrmion density. *Comput. Phys. Commun.* **260**, 107749 (2021).
39. Mermin, N. D. & Wagner, H. Absence of ferromagnetism or antiferromagnetism in one-or two-dimensional isotropic Heisenberg models. *Phys. Rev. Lett.* **17**, 1133 (1966).
40. Domenge, J.-C., Sindzingre, P., Lhuillier, C. & Pierre, L. Twelve sublattice ordered phase in the j 1- j 2 model on the kagomé lattice. *Phys. Rev. B-Condens. Matter Mater. Phys.* **72**, 024433 (2005).
41. Goerzen, M. A. *Thermal Equilibrium and Stability of Complementary Topological Solitons in Two-Dimensional Magnets*. Ph.D. thesis (Kiel University, 2024).
42. Müller, G. P. et al. Duplication, collapse, and escape of magnetic skyrmions revealed using a systematic saddle point search method. *Phys. Rev. Lett.* **121**, 197202 (2018).
43. von Malottki, S., Goerzen, M. A., Schrautzer, H., Bessarab, P. F. & Heinze, S. Eigenmode following for direct entropy calculation and characterization of magnetic systems. https://doi.org/10.48550/arXiv.2503.12109 (2025).
44. Henley, C. L. Ordering due to disorder in a frustrated vector antiferromagnet. *Phys. Rev. Lett.* **62**, 2056 (1989).
45. Grytsiuk, S. et al. Topological-chiral magnetic interactions driven by emergent orbital magnetism. *Nat. Commun.* **11**, 511 (2020).
46. Kurz, P. *Non-Collinear Magnetism at Surfaces and in Ultrathin Films*. Ph.D. thesis (RWTH Aachen, 2000).
47. Spethmann, J., Grünebohm, M., Wiesendanger, R., von Bergmann, K. & Kubetzka, A. Discovery and characterization of a new type of domain wall in a row-wise antiferromagnet. *Nat. Commun.* **12**, 3488 (2021).
48. Zahner, F. et al. Anisotropic atom motion on a row-wise antiferromagnetic surface. *Nat. Commun.* **16**, 4942 (2025).
49. Sessi, P., Guisinger, N. P., Guest, J. R. & Bode, M. Temperature and size dependence of antiferromagnetism in Mn nanostructures. *Phys. Rev. Lett.* **103**, 167201 (2009).
50. Zahner, F., von Bergmann, K., Wiesendanger, R. & Kubetzka, A. Reciprocity of magnetism and nanostructure growth. https://doi.org/10.48550/arXiv.2509.03202 (2025).
51. Alzate-Cardona, J., Sabogal-Suárez, D., Evans, R. & Restrepo-Parra, E. Optimal phase space sampling for Monte Carlo simulations of Heisenberg spin systems. *J. Phys. Condens. Matter* **31**, 095802 (2019).

Acknowledgements

We thank Felix Nickel, Tim Drevelow, Soumyajyoti Haldar, André Kubetzka and Kirsten von Bergmann for valuable discussions. This research was supported in part through high-performance computing resources available at the Kiel University Computing Centre. We gratefully acknowledge financial support from the Deutsche Forschungsgemeinschaft (DFG, German Research Foundation) via project no. 418425860 and no. 555842692. H.S. acknowledges financial support from the Icelandic Research Fund (grant No. 239435).

Author contributions

L.K. performed the Monte Carlo simulations. L.K. and S.H. analyzed the data. L.K. and M.A.G. developed the extension for the harmonic approximation. B.B. and H.S. implemented important parts of the code regarding the higher-order interactions and the numerical mode following algorithms. L.K. and S.H. wrote the manuscript with contributions from all authors.

Funding
Open Access funding enabled and organized by Projekt DEAL.

Competing interests
The authors declare no competing interests.

Additional information
Supplementary information The online version contains supplementary material available at https://doi.org/10.1038/s44306-025-00121-z.

Correspondence and requests for materials should be addressed to Leo Kollwitz.

Reprints and permissions information is available at http://www.nature.com/reprints

Publisher's note Springer Nature remains neutral with regard to jurisdictional claims in published maps and institutional affiliations.

Open Access This article is licensed under a Creative Commons Attribution 4.0 International License, which permits use, sharing, adaptation, distribution and reproduction in any medium or format, as long as you give appropriate credit to the original author(s) and the source, provide a link to the Creative Commons licence, and indicate if changes were made. The images or other third party material in this article are included in the article's Creative Commons licence, unless indicated otherwise in a credit line to the material. If material is not included in the article's Creative Commons licence and your intended use is not permitted by statutory regulation or exceeds the permitted use, you will need to obtain permission directly from the copyright holder. To view a copy of this licence, visit http://creativecommons.org/licenses/by/4.0/.

© The Author(s) 2025